High Precision Control for Off-Axis In-Situ Rotation of Nanorobot Inside SEM

Xiang Fu, Heng Zhang, Yuting Yang, Song Liu, and Yang Wang, *Member, IEEE*

***Abstract*—Robotic rotational nanomanipulation is crucial in fields like nanomaterial defect detection, nanoscale three-dimensional observation, and nanomaterial twisting characterization. In-situ rotation within a scanning electron microscope is challenging due to restricted workspace, limited field of view (FOV), depth of field (DoF), and large position shifts from rotation axis misalignment. Conventional solutions primarily employ nanorobots with extra structures to align the object with the rotation axis. However, this requires additional motion or observation units for the nanorobot, which either occupies multiple linear degrees of freedom or significantly consumes the limited workspace, thereby greatly impeding the dexterity. The novelty of this article resides in developing a control-oriented discrete time state-space model coupled with systematic calibration methodologies for axis and misalignment quantification. Through kinematic modeling rather than dynamic analysis, this approach enables real-time compensation of positional drift via outer-loop control strategies while maintaining compatibility with confined work space. Subsequently, we propose an iterative learning-based controller to enhance the response in subsequent iterations, thereby achieving high-precision off-axis in-situ rotation. Finally, a Barrier Lyapunov Function ensures the end-effector remains within the FOV and DoF, effectively mitigating visual servo singularities. Experimental validation against PID control and model predictive control demonstrates the strategy's stability, reliability, and superiority.**

***Index Terms*—Barrier Lyapunov function, in-situ nanomanipulation, iterative learning control (ILC), nanorobotics, off-axis rotation, scanning electron microscope (SEM).**

I. Introduction

IN-SITU manipulation within a scanning electron microscope (SEM) is pivotal in a wide range of applications, including nanoscale device fabrication [1], [2], [3], [4], cell manipulation [5], [6], [7], three-dimensional (3-D) nanoscale characterization [8], [9], [10], [11], [12], thus is broadly applied to materials science [13], [14], [15], [16], [17], [18], [19], [20], biology [5], [6], [7], and advanced manufacturing [1]. Despite the extensive research efforts and progress achieved so far in nanorobotics, the in-situ rotation within SEM remains unsolved stemmed from the restricted workspace, limited field of view (FOV) and depth of field (DoF) of the SEM, and larger position shifts caused by the misalignment of the end-effector or sample with respect to the rotation axis.

So far, considerable efforts have been dedicated to in situ rotation, employing primarily hardware-based strategies. One straightforward method is the integration of additional lenses. For example, Kasaya et al. [21] implemented an optical microscope alongside the SEM chamber, facilitating a supplemental side view that aids in the 3-D positioning of the end-effector within the SEM and enables the compensation of the position shift after each rotation. However, this approach can further restrict the available space within the SEM chamber and the hardware modification is difficult. As an alternative, recent research turns to the precise centering of the end-effector to the rotation axis. By mounting two linear nanopositioners orthogonally on the end of rotational nanopositioner, centering method is able to align the sample with the rotation axis during the rotation, thus mitigating substantial displacement. For example, the authors in [22], [23], and [24] introduced alignment strategies known as triple-image alignment (TIA). By assuming the rotation axis to be orthogonal to the two linear moving axes, TIA simplifies the modeling process, although it inherently introduces model errors. Additionally, the alignment technique necessitates the use of two linear nanopositioners specifically tailored for centering, which consequently restricts the ability to perform complex rotary manipulations, such as tension testing of micromaterials [25] and other specialized applications [26]. In summary, existing solutions primarily rely on reconfiguring the hardware, either by incorporating auxiliary vision equipment within the chamber or by attaching additional linear nanopositioners to a rotational nanopositioner. Such modifications inevitably increase the complexity and cost of the nanorobot system and diminish the manipulation flexibility. For the classical nanorobot setup inside SEM considered in this article, without modifications to the hardware, there is no viable solution for addressing the challenges of off-axis in-situ rotation yet.

The classical nanorobot inside SEM examined in this article features a conventional setup, comprising three orthogonally arranged linear nanopositioners and a rotational nanopositioner

Received 30 August 2025; accepted 22 November 2025. Recommended by Technical Editor J. Ren and Senior Editor K. Oldham. This work was supported by the National Natural Science Foundation of China under Grant 62503329, Grant 62303321, and Grant T2522022. *(Xiang Fu and Heng Zhang contributed equally to this work.) (Corresponding authors: Song Liu; Yang Wang.)*

The authors are with the School of Information Science and Technology, ShanghaiTech University, Shanghai 201210, China (e-mail: fuxiang2022@shanghaitech.edu.cn; zhangheng1@shanghaitech.edu.cn; yangyt1@shanghaitech.edu.cn; liusong@shanghaitech.edu.cn; wangyang4@shanghaitech.edu.cn).

This article has supplementary material provided by the authors and color versions of one or more figures available at https://doi.org/10.1109/TMECH.2025.3640929.

Digital Object Identifier 10.1109/TMECH.2025.3640929

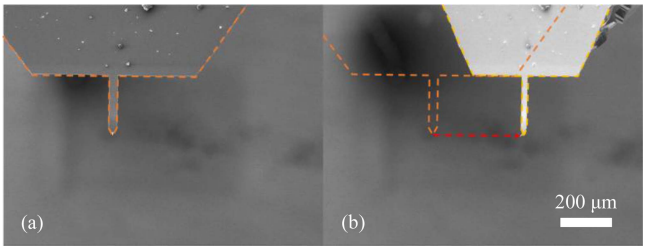

Fig. 1. Position shift caused by misalignment of cantilever with respect to the rotation axis, where the magnification is 100×, and the scale bar is 200 μm. (a) SEM image of cantilever before rotation. (b) SEM image of cantilever after rotation of 50°.

at the end of the arm [27], [28]. The SEM positioned above captures 2-D images of the workspace, providing monocular visual feedback. This setup allows for high controllability and flexibility to carry out complex and dynamic maneuvers in 3-D space. Modern nanorobot systems can easily achieve reliable high precision linear movements [29] though, to realize high precision in situ rotation with a classic nanorobot setup is still rather challenging, mainly due to two factors: First, the end-effector or sample inevitably displaces away from the rotation axis, a phenomenon termed as off-axis rotation [25]. Second, there is an unignorable mechanical deviation of the rotation axis of the rotary nanopositioner caused by nanorobot manufacturing process [25], [26]. As a result, as illustrated in Fig. 1, even a small rotational angle could induce significant position shifts on the order of hundreds of microns. Large position shift would further induce the sample or end-effector to move outside the FOV or beyond the DoF of SEM, resulting in the problem of visual servo singularity issues [30]. In addition, in complicated manipulation tasks inside SEM, like nanodevice fabrication [1], unexpected or unpredictable large position shift may probably lead to collision of the end effector with object. All these factors highlight the challenging and necessity for real-time compensation to maintain accuracy during off-axis in-situ rotation inside SEM.

In response, this article presents an alternative framework that encompasses new modeling, calibration, and control strategies achieving ultra-high precision off-axis in situ rotation for classic nanorobot setup under SEM. *Our approach diverges from conventional methods by establishing a novel control-oriented mathematical framework capable of compensating feature-point positional shifts during off-axis rotations through outer-loop controller design, thereby obviating hardware modifications.* Conventional robotics modeling and control approaches predominantly emphasize dynamic refinement of the inner-loop PID controller, as evidenced in prior articles [22], [24]. While the inner-loop guarantee micron-level precision in a single motion stage, it fails to ensure high-precision composite motion involving rotation due to inherent manufacturing and assembly tolerances in the outer-loop mechanical chain. To this end, we first shift focus to the outer loop and derive a new control-oriented discrete time state-space model (SSM) grounded in kinematics. The key characteristic of the model is that it enables the online compensation for the position shift via three linear nanopositioner in the outer loop. The accuracy of the SSM is further improved by a series of systematic calibration techniques for calibrating the rotation axis and identifying the misalignment between the axis and the target point. Then, building on the control-oriented SSM, we propose a high-order iterative learning control (ILC) method, fully leveraging repetitive nature of the off-axis in situ rotations. Other control techniques like sliding mode control [31], adaptive control [32], and MPC tactics [33], although effective in many macroscopic robot systems, are inadequate for this problem due to the high-precision requirement and limited workspace. These methods often suffer from the chattering phenomenon, large overshoot, and parameter drift, or demand high model precision. Instead, the proposed control strategy fully utilizes data from previous operations to incrementally refine the control inputs, thereby achieving high precision off-axis in-situ rotation. Additionally, we incorporate a Barrier Lyapunov Function (BLF) into the control algorithm to ensure that the end-effector is always kept within the FOV and DoF of SEM, effectively mitigating the risk of visual servo singularity problem and ensuring a stable, reliable manipulation process. Experimental results from in-situ rotations illustrate a drastic reduction in the average position shift of the target object from 478.310 to 0.309 μm at step size of 0.5°, reflecting an enhancement in precision of 99.935% , while a PID controller achieved a precision of 0.815 μm and an MPC controller attained a precision of 0.822 μm. The BLF term was also validated to remain within the FoV boundary.

In light of the challenges posed by off-axis in-situ rotation within the restrictive environment of SEM, this article efforts contribute in several aspects.

1) We propose a complete framework, including new modeling, calibration, and control strategies, to achieve ultra-high precision off-axis in-situ rotation deployable to a classic nanorobot setup under SEM.
2) We propose a control-oriented discrete-time SSM along with a systematic calibration technique to align theoretical constructs with real-world robot dynamics. This model, based on kinematics rather than dynamics, enables online compensation of position shifts via outer loop control. Consequently, the classic nanorobot is preserved, eliminating the need for extra hardware reconfigurations.
3) We propose a high-order ILC strategy equipped with a BLF-based term. The incorporation of constraint parameters ensures that the end-effector is always kept within the FOV and DoF of the SEM, effectively mitigating the risk of visual servo singularity.

The rest of this article is organized as follows. In Section II, the system configuration and displacement investigation are first discussed followed by the modeling of the nanorobotic system and the calibration for misalignment and rotation axis is clarified. Then, in Section III, the high-order ILC strategy equipped with a BLF-based term is proposed. The reliability and availability of the proposed approach is validated by well-designed experiments and is compared with the state-of-the-art methods in Section IV. Finally, Section V concludes this article.

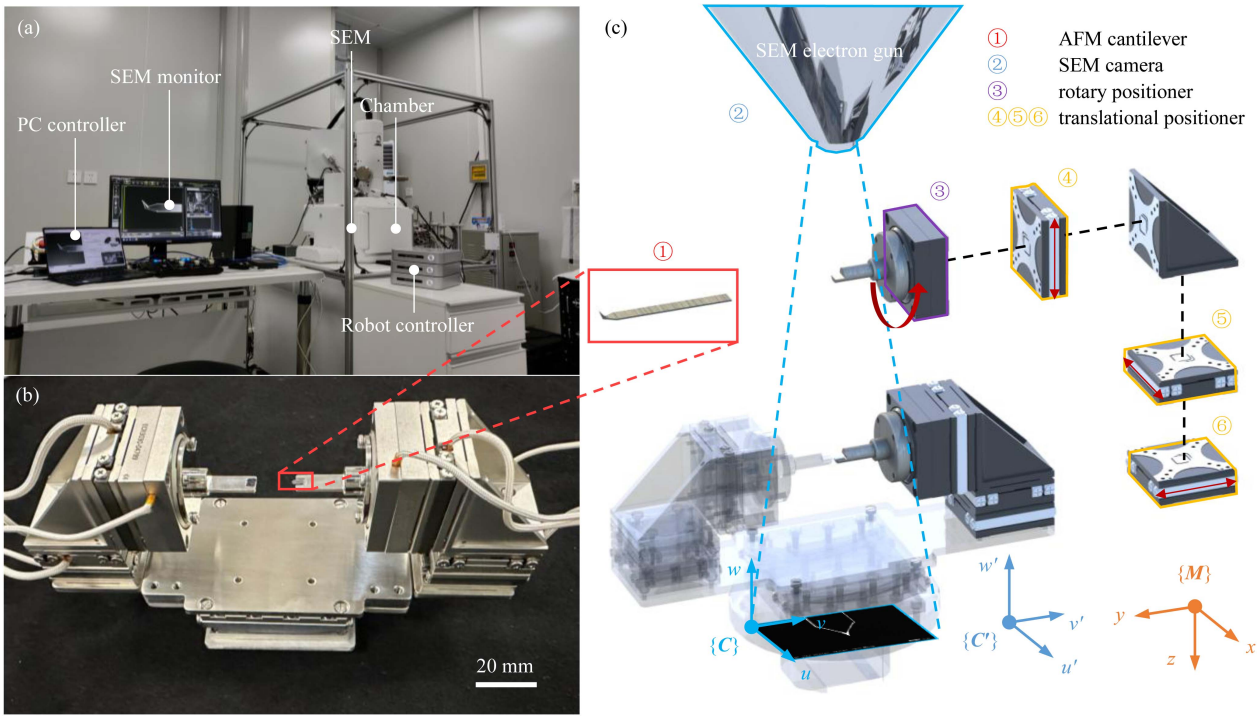

Fig. 2. Configuration of the classical nanorobotic manipulation system integrated with a JEOL JSM-IT500HR/LA InTouchScope SEM. (a) Overview of system where a dedicated port is engineered to link the nanorobot with the external environment encompassing control and power units. (b) Experimental nanomanipulation platform equipped with ECS × 3030, ECR3030 nanopositioners (Attocube Systems AG). An AFM cantilever serves as the robot's end-effector for in-situ point rotation control validation. (c) Schematic illustration of the nanorobot containing three translational DOFs and one rotary DOF, along with the corresponding coordinate systems.

II. Rotational Nanorobotic Manipulation System and Modeling

A. Nanorobotic Manipulation System

Configuration of the nanorobotic manipulation system considered in this article is illustrated in Fig. 2, which consists of an SEM camera and four nanopositioners. A dedicated port is engineered to link the robot with the external environment, encompassing both the operator and the control system.

The SEM camera is a top-view camera that transforms the incremental translational motion of object from the 3-D Cartesian space { $\boldsymbol{M}$ } into its representation in the image space { $\boldsymbol{C}$ }. Specifically, the 3-D motion space { $\boldsymbol{M}$ } is defined on the base of robotics system, with x-, y-, and z-axes aligned with the orientations of three translational nanopositioners. The image space { $\boldsymbol{C}$ } is established on the imaging plane of SEM camera, where u- and v-axes represent two axes of SEM image and w-axis represents the optical axis, which is orthogonal to u- and v-axes. In this article, a cantilever is used to present the object, which also serves as the end-effector. The movement of the cantilever is conducted by four nanopositioners: three orthogonally mounted linear nanopositioners, and one rotary nanopositioner utilized at the end of the nanorobotic manipulation arm.

B. Investigation of the Position Shift During Off-Axis Rotation

Four nanopositioners provide three translational DOFs (repetitive precision of 50 nm) and one rotary DOF (repetitive angle precision of up to 1 millidegree). High precision movement is guaranteed by a stepper motor based on a grating encoder. Nevertheless, this does not ensure high-precision of the in-situ rotation. Because, in a rotary machine, the radial run-out usually exists due to machining error [24], which is considered as a main cause of unpredictable position shift of the cantilever during the off-axis rotation.

As shown in Fig. 3 , the y-axis in { $\boldsymbol{M}$ } is not the rotation axis, despite its close proximity. Together with the fact that the cantilever consistently maintains a misalignment from the rotation axis, i.e., the in-situ rotation is off-axis, as shown in Fig. 1, there are significant position shifts at the microscale, even when the rotation angle is small [see Supplementary Information (SI) I for more detail]. Such shifts become problematic when conducting sustained rotational manipulation, as it may cause the cantilever to move out of the FoV or DoF, which is known as the visual servo singularity problem. This problem is one of the key challenges faced by in-situ rotation using the classical nanorobot system in SEM, and will be addressed by the proposed framework without any hardware modification.

C. State-Space Modeling and Calibration

The considered nanorobot system employs a dual-loop control architecture. The inner loop governs dynamic regulation of the robotic hardware through a grating encoder and PID controller to ensure precise stepper motor actuation. The outer loop, operating on the inner loop's output, executes position servoing by adjusting robotic displacements in accordance with

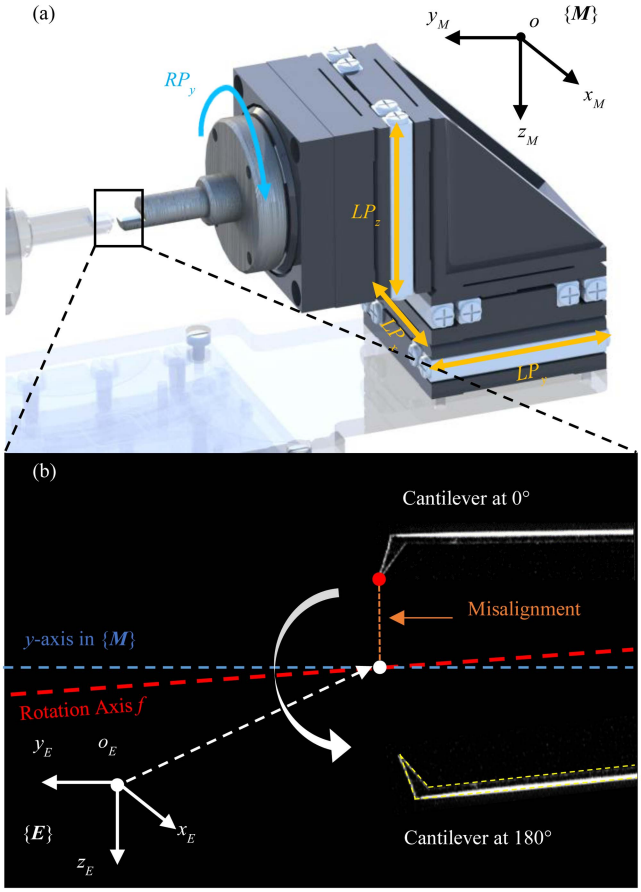

Fig. 3. (a) Diagram of nanorobot system configuration. (b) Schematic illustration of the position shift during the off-axis rotation. Note that the rotation axis *f* is close to, but not aligned with, the *y*-axis in {***M***}. There is a significant misalignment between the cantilever and the rotation axis *f*, which is defined as perpendicular to the *y*-axis.

the kinematic model and SEM visual feedback. Conventional robotics modeling and control approaches predominantly emphasize dynamic refinement of the inner-loop PID controller, as evidenced in prior articles [22], [24]. In this article, we shift focus to the outer loop (detailed in SI Section II-A), constructing a discrete-time SSM grounded in kinematics. This methodology establishes a novel control-oriented mathematical framework capable of compensating feature-point positional shifts during off-axis rotations through outer-loop controller design, thereby obviating hardware modifications.

First, we introduce two auxiliary coordinates { $\boldsymbol{C}'$ } and { $\boldsymbol{E}$ } to facilitate the utilization of standard rotation matrix in (1). Specifically, the orientation of the axes of { $\boldsymbol{C}'$ } is chosen to be same as that of { $\boldsymbol{C}$ } while the scale in { $\boldsymbol{C}'$ } is set to be the same as in { $\boldsymbol{M}$ }. The origin of { $\boldsymbol{E}$ } is positioned at a certain point of the rotation axis so that the tracked feature point lies on x–z plane in { $\boldsymbol{E}$ }, and the orientation of three axes of { $\boldsymbol{E}$ } are aligned with { $\boldsymbol{M}$ }. Primarily, { $\boldsymbol{E}$ } does not move or rotate relative to the { $\boldsymbol{M}$ } during the rotation process, i.e., as the linear nanopositioner moving, the origin of { $\boldsymbol{E}$ } remains fixed in { $\boldsymbol{M}$ }. { $\boldsymbol{E}$ } puts the emphasis on the misalignment between the cantilever and the rotation axis.

Based on the established coordinates systems, the SSM (derivation detail see SI Section II-B) of the nanorobotic manipulation system that governs the transformation the position of tracked feature point form the time instant t—1st step to tth step, is constructed as

$$\begin{cases} \boldsymbol{X_t} = \boldsymbol{R}(f,\Delta\theta)\boldsymbol{X_{t-1}} + \boldsymbol{u_t} \\ +(\boldsymbol{I} - \boldsymbol{R}(f,\Delta\theta))\sum_{n=0}^{t-1}\boldsymbol{u_n} + \boldsymbol{\delta_t} \\ \boldsymbol{X_0} = \begin{bmatrix}\Delta x_f & \Delta y_f & \Delta z_f\end{bmatrix}^T, \boldsymbol{u_t} = \begin{bmatrix}{u_x}^t & {u_y}^t & {u_z}^t\end{bmatrix} \end{cases} \tag{1}$$

where the vector $[\Delta x_f\ ,\ \Delta y_f\ ,\ \Delta z_f\ ]^{\mathrm{T}}$ denotes the systematic misalignment, and at tth time step, $\boldsymbol{X_t} = [{P_x}^t\ ,\ {P_y}^t\ ,\ {P_z}^t\ ]^{\mathrm{T}}$ represents the position of a user-defined feature point to be tracked on the cantilever, $\boldsymbol{u_t}$ represents the translation motion of the linear nanopositioners, and δ_t stands for the influence brought by the extra additive Guassian noise $\mathcal{N}_a$. $\Delta\theta := \theta_t - \theta_{t\ -1}$ is the rotation angle for each step, which is generally constant during the in-situ rotational manipulation. $\boldsymbol{X_0}$ is the initial condition of SSM (1) as well as the target position of the in-situ rotation manipulation. $\boldsymbol{R}\ (f,\ \theta_t\ )$ is the conventional rotation matrix [34] around rotation axis f with respect to the rotation angle θ_t at tth time step. $\boldsymbol{R}\ (f,\ \Delta\theta)$ is denoted as $\boldsymbol{R}$ in the forthcoming sections for simplicity.

Now, by regarding $\boldsymbol{u_t}$ as the control input and δ_t as the external disturbance, SSM (1) clearly provides a control-oriented mathematical model. While this model is compatible with generic controller implementations [35], [36] like PID controller and MPC [33], we further propose an ILC in the following section that systematically exploits the repetitive nature of in situ rotation tasks to enhance operational precision. In addition to a proper controller design, an effective compensation also relies on accurate identification of the vector $[f_x\ ,f_y\ ,f_z\ ]^{\mathrm{T}}$ and the vector $[\Delta x_f\ ,\ \Delta y_f\ ,\ \Delta z_f\ ]^{\mathrm{T}}$ that can be obtained through the calibration of the initial position of the tracked feature point and the rotation axis, respectively. Due to the limitation of the space, the details on modeling derivation and calibration methods are presented in the SI Section III, consisting of the systematic misalignment recognition and rotation axis calibration.

III. Iterative-Learning-Based High-Order Feedback Control for On-Line Compensation

A. Formulation of Control Problem and Output Constraints

Based on the SSM (1), achieving high-precision off-axis in-situ rotation can be reformulated into an output regulation problem in which the goal is to design a control law $\boldsymbol{u_t}$ that ensures the output of the system $\boldsymbol{X_t}$ follows a desired reference signal $\boldsymbol{X_0}$ despite uncertainties in the system model or external disturbances. To enhance precision, here we leverage the repeatability of the in-situ rotational manipulation and innovatively employ the idea of iterative learning (IL) to gradually reduce the offset between $\boldsymbol{X_t}$ and $\boldsymbol{X_0}$ after each round of rotation then ultimately achieving high-precision performance. The iterative nature of this approach allows the controller to compensate for model uncertainties and unmodeled dynamics by extensively utilizing information from previous iterations,

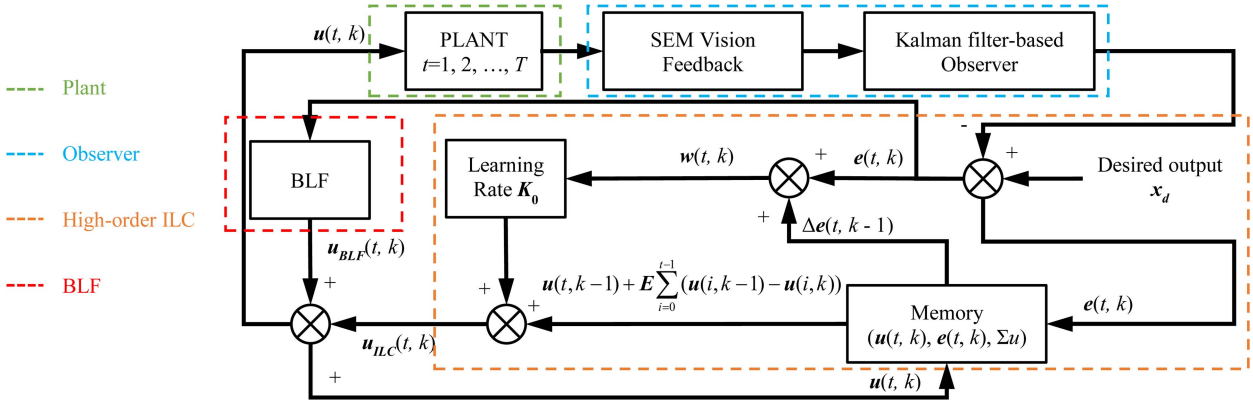

Fig. 4. Block diagram of the control system containing the plant, observer and BLF-integrated iterative learning controller.

which is particularly useful for the in-situ rotation task as when we consider a 360° rotation of the cantilever as one iteration.

To facilitate the IL-based compensating strategy, we denote the number of iterations by the variable k, allowing us to rewrite the SSM in (1) in the following form:

$$\begin{aligned} \boldsymbol{X}(t+1,k) &= \boldsymbol{A}\boldsymbol{X}(t,k) + \boldsymbol{B}\boldsymbol{u}(t,k) \\ &\quad + \boldsymbol{E}\sum_{i=0}^{t-1}\boldsymbol{u}(i,k) + \boldsymbol{\delta}(t,k) \\ \boldsymbol{Y}(t+1,k) &= \boldsymbol{C}\boldsymbol{X}(t+1,k) \end{aligned} \tag{2}$$

where

$$\boldsymbol{A} \equiv \boldsymbol{R}(f,\Delta\theta), \boldsymbol{B} \equiv \boldsymbol{I}_{3\times 3}, \boldsymbol{E} \equiv \boldsymbol{I} - \boldsymbol{R}(f,\Delta\theta), \boldsymbol{C} \equiv \boldsymbol{J}_{\boldsymbol{C}} \tag{3}$$

and $\boldsymbol{X}(t,k)$ represents the state of the system at tth step in the kth iteration, with $t \in \{0,1,2,\ldots,T\}$ and $k \in \{0,1,2,\ldots\}$ where T is the number of steps in one iteration.

For system (2), the off-axis in-situ rotation task for the nanorobot system can now be formally formulated as: finding a proper control law $u(t, k)$ under model uncertainties and external disturbances $\delta(t, k)$ such that the output state $X(t + 1, k)$ can be maintained as close as possible to the initial position $X(0, 0) = X_0$. Additionally, to enable the feedback controller design based on the information provided by SEM, we need to ensure position of cantilever within the FoV of the SEM, that is the controller must also ensure that $|Y(t, k) - Y(0, 0)| \leq r$, where r is a user-defined value which must be set smaller than the radius of the FOV.

B. IL-Based High-Order Controller Design

For the control problem stated in Section III-A, we propose the following high-order ILC strategy as demonstrated in Fig. 4:

$$\begin{aligned} \boldsymbol{u}(t,k) &= \boldsymbol{u}(t,k-1) + \boldsymbol{K_0}\cdot\boldsymbol{w}(t,k) \\ &\quad + \boldsymbol{E}\sum_{i=0}^{t-1}(\boldsymbol{u}(i,k-1) - \boldsymbol{u}(i,k)) \end{aligned} \tag{4}$$

where $\boldsymbol{u}(t, k)$ represents the compensation input at the tth step of the kth iteration and $\boldsymbol{K_0}$ is a 3-by-3 gain matrix satisfying $0 < \beta = \rho(\boldsymbol{I} + \boldsymbol{B}\boldsymbol{K_0}) + \kappa < 1$for a small constant $\kappa>0$. $\boldsymbol{w}(t, k)$ is a full-state error signal delineated as follows:

$$\boldsymbol{w}(t,k) = \boldsymbol{e}(t,k) + \Delta\boldsymbol{e}(t,k-1) \tag{5}$$

where the tracking error $\boldsymbol{e}(t,k) = \boldsymbol{X_d}(t) - \boldsymbol{X}(t,k)$ with $\boldsymbol{X_d}(t)$ representing the desired position at tth step. In terms of in-situ rotation, the desired position $\boldsymbol{X_d}(t) = \boldsymbol{X}(0, 1) = \boldsymbol{X_0}$.

Note that, in contrast to the conventional ILC [34], here, the feedback error $\boldsymbol{w}(t, k)$ in (5) concerns not only the displacement in the last iteration but also accounts for the error in the current iteration, which motivates the term of "high-order feedback." The state vector $\boldsymbol{X}(t, k) = \hat{\boldsymbol{X}}_{t-1}$ at ith step of a certain iteration is provided by a standard Kalman filter as follows (for notational simplicity, the iteration number k is ignored):

$$\text{predictor} \begin{cases} \hat{\boldsymbol{X}}_{\boldsymbol{t}}^{-} = \boldsymbol{A}\hat{\boldsymbol{X}}_{\boldsymbol{t-1}} + \boldsymbol{B}\boldsymbol{u_t} + \boldsymbol{E}\sum_{n=0}^{t-1}\boldsymbol{u_n} \\ \boldsymbol{P}_{\boldsymbol{t}}^{-} = \boldsymbol{A}\boldsymbol{P}_{\boldsymbol{t-1}}\boldsymbol{A}^T + \boldsymbol{Q}^* \end{cases} \tag{6}$$

$$\text{observation} \boldsymbol{Y}_t = \boldsymbol{C}\boldsymbol{X}_t \tag{7}$$

$$\text{corrector} \begin{cases} \boldsymbol{K_t} = \boldsymbol{P}_{\boldsymbol{t}}^{-}\boldsymbol{C}^T(\boldsymbol{C}\boldsymbol{P}_{\boldsymbol{t}}^{-}\boldsymbol{C}^T + \boldsymbol{R}^*)^{-1} \\ \hat{\boldsymbol{X}}_{\boldsymbol{t}} = \hat{\boldsymbol{X}}_{\boldsymbol{t}}^{-} + \boldsymbol{K}_t(\boldsymbol{Y}_t - \boldsymbol{C}\hat{X}_{\boldsymbol{t}}^{-}) \\ \boldsymbol{P_t} = (\boldsymbol{I} - \boldsymbol{K_t}\boldsymbol{C})\boldsymbol{P}_{\boldsymbol{t}}^{-} \end{cases} \tag{8}$$

where $\hat{\boldsymbol{X}}_{t-1}$ is the estimation of the position of the tracked feature point at time step $t-1$, and $\hat{\boldsymbol{X}}_{\boldsymbol{t}}^{-}$ represents the position of the tracked feature point at time step t purely based on the SSM (1). $\boldsymbol{u_t}$ is the input signal at tth step, as defined above in (4). $\boldsymbol{Y_t}$ is the position of the tracked feature point projected onto the image plane, where the origin is aligned with the origin of the coordinate system $\{\boldsymbol{E}\}$. $\boldsymbol{Y_t}$ can be calculated as follows:

$$\boldsymbol{Y}_t = \boldsymbol{y}_t - \boldsymbol{y_d} + \boldsymbol{C}\cdot\boldsymbol{X}_0 \tag{9}$$

where $\boldsymbol{y_t}$ is the position on image plane at tth step and $\boldsymbol{y_d}$ is the desired output that equals the initial position of the tracked feature point projected onto the image plane. The matrix $\boldsymbol{Q}^* \in \mathbb{R}^{3\times 3}$ denotes the process noise covariance, which captures modeling errors and external disturbances, while $\boldsymbol{R}^* \in \mathbb{R}^{3\times 3}$ represents the measurement noise covariance, reflecting the statistical characteristics of sensor uncertainties. Proper tuning of $\boldsymbol{Q}^*$and $\boldsymbol{R}^*$ is essential for improving estimation accuracy and

ensuring robustness against noise and model uncertainties. In this article, the values of $\boldsymbol{Q}^*$and $\boldsymbol{R}^*$ used in our implementation are provided in the experimental section. Clearly, the estimation of the position $\boldsymbol{X_t}$ is obtained by a weighted combination of the prediction and observation. Due to space limitations, the standard convergence analysis [37] of the Kalman filter is not presented here. The estimation of position through Kalman filter then facilitates full-state feedback compensation.

Finally, it is worth mentioning that in the first iteration, only the displacement on the current tth step is available, hence, with the aid of calibration in Section II-C, the initial input is as follows:

$$\boldsymbol{u}(t,1) = (\boldsymbol{I} - \boldsymbol{R}(f, t\cdot\Delta\theta))\cdot\boldsymbol{X_0} + \boldsymbol{K_0}\cdot\boldsymbol{w}(t,k) \tag{10}$$

where $t\cdot\Delta\theta$ is the rotation angle at tth step. A rigorous stability analysis of the overall system under the proposed controller is presented in SI Section IV-A, which theoretically ensures the effectiveness of the proposed compensation algorithm for achieving high-precision off-axis in-situ rotation. In short, with our designed controller: in the absence of external disturbance $\delta(t,k)$, the tracking error of the system states converges globally and asymptotically to zero; when system (2) is subject to norm-bounded external disturbances $\delta(t,k)$, the proposed HOILC still ensures that the system states converge to the neighborhood of the desired states.

C. Incorporation of the Barrier Lyapunov Function

The control law (4) can achieve off-axis in-situ rotational motion and ensure all states are bounded. However, this does not guarantee that the cantilever will not exceed FoV during rotation, which is a necessary condition for the continuation of the rotational manipulation under SEM. Therefore, in this section, we expand our IL-based controller by incorporating a BLF-based term to ensure that $\boldsymbol{X}(t,k)$ always remains within the user-defined constraints. More detailed preliminary on BLF can be found in SI Section IV-B.

For the sake of analysis, we first rewrite (2) in the text as

$$\begin{aligned}\boldsymbol{X}(t+1,k) &= \boldsymbol{A}\boldsymbol{X}(t,k) + \boldsymbol{B}\boldsymbol{v}(t,k) + \boldsymbol{\delta}(t,k)\\ \boldsymbol{Y}(t+1,k) &= \boldsymbol{C}\boldsymbol{X}(t+1,k)\end{aligned} \tag{11}$$

where

$$\boldsymbol{v}(t,k) = \boldsymbol{u}(t,k) + \boldsymbol{E}\sum_{i=0}^{t-1}\boldsymbol{u}(i,k). \tag{12}$$

Now, we propose the BLF-incorporated ILC as follows:

$$\boldsymbol{v}(t,k) = \boldsymbol{v}_{\mathrm{ILC}}(t,k) + \boldsymbol{v_{BLF}}(t,k). \tag{13}$$

It can be seen that controller (11) consists of two parts. One part is the ILC algorithm proposed above, which we restate here

$$\begin{aligned}\boldsymbol{v_{ILC}}(t,k) &= \bar{\boldsymbol{v}}(t,k) + \boldsymbol{K_0}\boldsymbol{X}(t,k)\\ \bar{\boldsymbol{v}}(t,k+1) &= \bar{\boldsymbol{v}}(t,k) + \boldsymbol{K_0}(\boldsymbol{X}(t+1,k) - \boldsymbol{X_d}(t+1))\end{aligned} \tag{14}$$

where $\boldsymbol{K_0}$ is a 3-by-3 matrix defined in (4). The remaining part of (11), $\boldsymbol{v_{BLF}}(t,k)$, is now given as follows:

$$\boldsymbol{v_{BLF}}(t,k) = \begin{cases} -\hat{\boldsymbol{\delta}}(t,k) - K_2\frac{\boldsymbol{\alpha}^{\mathrm{T}}\delta_1\|\boldsymbol{e}(t,k)\|}{\|\boldsymbol{\alpha}\|} & \text{if}\boldsymbol{\alpha}\neq 0\\ -\hat{\boldsymbol{\delta}}(t,k) & \text{if}\boldsymbol{\alpha}=0\end{cases}$$

$$\hat{\boldsymbol{\delta}}(t,k) = P[\hat{\boldsymbol{\delta}}(t+1,k-1)] + K_1\boldsymbol{\alpha}^{\mathrm{T}} \tag{15}$$

where K_1 and K_2 are positive constant control gains, and α is defined as

$$\boldsymbol{\alpha} := \frac{\partial V(\boldsymbol{e})^{\mathrm{T}}}{\partial \boldsymbol{e}(t,k)} = \frac{\boldsymbol{e}(t,k)^{\mathrm{T}}}{\cos^2\left(\frac{\pi\boldsymbol{e}(t,k)^{\mathrm{T}}\boldsymbol{e}(t,k)}{2k_b{}^2}\right)} \tag{16}$$

with $\hat{\boldsymbol{\delta}}(t,0) = 0$ for all $t\in\{0,1,2,\ldots,T\}$, δ_1 is the constant. In this article, we choose the tan-type barrier function as $V(\boldsymbol{e})$, but the others, including the natural logarithmic type one, are also applicable. $P[\hat{\boldsymbol{\delta}}]$ represents the projection operations on each element of $\hat{\boldsymbol{\delta}} := [\hat{\boldsymbol{\delta}}_1 \quad \hat{\boldsymbol{\delta}}_2 \quad \hat{\boldsymbol{\delta}}_3]^{\mathrm{T}}$, namely

$$P(\hat{\boldsymbol{\delta}}) = \left[P(\hat{\boldsymbol{\delta}}_1) \quad P(\hat{\boldsymbol{\delta}}_2) \quad P(\hat{\boldsymbol{\delta}}_3)\right]^{\mathrm{T}}$$

$$P(\hat{\boldsymbol{\delta}}_{\boldsymbol{i}}) = \begin{cases}\hat{\boldsymbol{\delta}}_{\boldsymbol{i}} & \left|\hat{\boldsymbol{\delta}}_{\boldsymbol{i}}\right| \le \bar{\hat{\boldsymbol{\delta}}}_{\boldsymbol{i}}\\ \mathrm{sign}(\hat{\boldsymbol{\delta}}_{\boldsymbol{i}})\bar{\hat{\boldsymbol{\delta}}}_{\boldsymbol{i}} & \left|\hat{\boldsymbol{\delta}}_{\boldsymbol{i}}\right| > \bar{\hat{\boldsymbol{\delta}}}_{\boldsymbol{i}}\end{cases},\ i=1,2,3$$

where $\bar{\hat{\boldsymbol{\delta}}}_{\boldsymbol{i}}$is the estimated upper bounds of external disturbance $\delta(t,k)$. From (16), one can see that α goes to infinity as the norm of the system error $\boldsymbol{e}(t,k)$ approaches the boundary k_b, i.e., $\|\boldsymbol{e}(t,k)\| \to k_b$. The BLF term endows the proposed controller with the property that, as $\boldsymbol{e}(t,k)$ increases, the control input will increase correspondingly, thereby forcing the system state to remain near the desired state. Therefore, the cantilever is ensured to remain within the FoV, and ensure the position of tracked feature point to be observed by SEM accurately.

It should be noted that the output of the designed controller is not the true input of system (1); in experiments, it is necessary to convert $\boldsymbol{v}(t,k)$ into $\boldsymbol{u}(t,k)$ through the transformation operation in (12), which is then used as the actual input for the nanopositioners. It should be noted that the theoretical derivation of the proposed algorithm does not impose an upper bound constraint on the input; however, in practical engineering applications, it is necessary to ensure that the actual allowable upper bound of the input is far larger than the variation range of the system state. Failure to meet this condition may have an adverse impact on the convergence characteristics of the algorithm. For potential integral windup issues, readers may refer to existing controller design schemes that account for input constraints, e.g., [38].

IV. Experiment and Results

A. Experimental Setup

1) Hardware Configuration: As shown in Fig. 2, the SEM used in this system is JEOL JSM-IT500HR/LA, operating in high vacuum mode to image samples by detecting secondary electrons, under 10 kV acceleration voltage, which captures 7 frames per second (frame/s) with image size of 640 × 480 pixel.

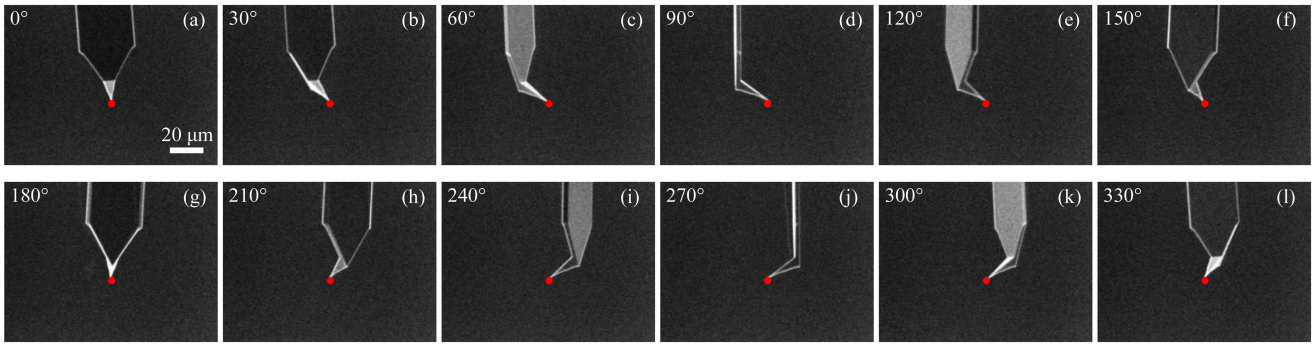

Fig. 5. SEM images of a cantilever's in-situ rotating with the proposed controller and rotation range of 360°, rotation step size of $\Delta\theta$ =1°. The magnification is 1000× and the length of scale bar is 20 μm. (a) $\theta = 0°$. (b) $\theta = 30°$. (c) $\theta = 60°$. (d) $\theta = 90°$. (e) $\theta = 120°$. (f) $\theta = 150°$. (g) $\theta = 180°$. (h) $\theta = 210°$. (i) $\theta = 240°$. (j) $\theta = 270°$. (k) $\theta = 300°$. (l) $\theta = 330°$. The AFM cantilever used here is NANOSENSORS ATEC-FM. The red dot represents the initial position of the cantilever tip.

The cantilever employed in this experiment was NANOSENSORS ATEC-FM, as shown in Fig. 5. The position of tracked feature point is monitored through edge point detection using the Canny operator [39], implemented with a strong threshold of 100 and a weak threshold of 180. SEM provides images of 192 × 256, 96 × 128, and 48 × 64 μm FoV at magnification of 500, 1000, and 2000, respectively. Hence, the observed sample may move out of FoV when the position error is larger than 128, 64, and 32 μm for magnification of 500, 1000, and 2000, respectively.

The translational nanopositioners, which are orthogonally mounted in this nanorobotic manipulation system, were Attocube piezoelectric ECS × 3030, representing x-, y-, and z-axes. The rotational nanopositioner is an Attocube piezoelectric ECR3030, with the rotation axis situated close to y-axis in $\{\boldsymbol{M}\}$. The translational positioners offer repeatability precision of 50 nm, while the rotary nanopositioner achieves a repetitive angle precision of up to 1 millidegree. The employed voltage is 35 V.

2) Calibration Results: To calibrate the initial misalignment, we implement the methodology detailed in SI Section III through eight movement trials involving a rotation of 15°. This process yields the initial misalignment vector $[\Delta x_f\ ,\ \Delta y_f,\ \Delta z_f]^{\mathrm{T}} = [248949,\ 0,\ 642078]^{\mathrm{T}}$ nm and vector $\boldsymbol{f}_M = [0.098,\ -0.9999,\ 0.0098]^{\mathrm{T}}$. Additionally, the rotation axis is observed to closely align with the y-axis in $\{\boldsymbol{M}\}$, signifying that the offset is more pronounced along the u-axis in the image space $\{\boldsymbol{C}\}$. Finally, the image Jacobian matrix can be computed based on the calibrated Jacobian matrix and the applied magnification [29]. For instance, for the experiments conducted in this article at a magnification of 1000, the image Jacobian matrix is established as follows:

$$\boldsymbol{J_C} = \begin{bmatrix} 2.20e-4 & 5.07e-3 & -6.25e-5 \\ 5.11e-3 & -8.66e-5 & -5.00e-6 \\ -3.08e-8 & -3.18e-7 & -2.59e-5 \end{bmatrix} \text{ pixel/nm}.$$

3) Parameters Setting: To validate the efficiency of our system under various working conditions, we conducted experiments at different control step sizes and magnifications. Specifically, the SEM magnifications were set to 500×, 1000×, and 2000×. Three distinct step sizes, namely 0.5°, 1°, and 5°, were selected. The detailed parameters of the control algorithm used are as follows. First, the control gain, denoted as $\boldsymbol{K_0}$, is set to be diag{0.9, 0.9, 0.9}. As for BLF-related parameters, $K_1 = 0.001$, $K_2 = 1$, and $\delta_1 = 0.23$. The output constraints k_b for 500×, 1000×, and 2000× are set to be 150 000, 75 000, and 37 500 nm, respectively. Regarding to the Kalman filter, the values on the diagonal of $\boldsymbol{Q}^*$ are uniformly set to 10^5, while the values on the diagonal of $\boldsymbol{R}^*$ are all set to 1.

4) Evaluation Metric: To properly assess the performance of the rotary manipulation, we calculate the positional shift of tth step, denoted as SFT(t), obtained from the SEM images and calculate the average position shift $\mathrm{SFT}_{\mathrm{avg}}$, during the entire rotating process as follows:

$$\mathrm{SFT}(t) = \left\| \boldsymbol{J_C}^{-1} \left(\begin{bmatrix} u_P(t) \\ v_P(t) \\ 0 \end{bmatrix} - \begin{bmatrix} u_{\mathrm{target}} \\ v_{\mathrm{target}} \\ 0 \end{bmatrix} \right) \right\|_2,$$

$$\mathrm{SFT}_{\mathrm{avg}} = \frac{1}{T} \sum_{t=1}^{T} \mathrm{SFT}(t)$$

where $\boldsymbol{J_C}$ is the image Jacobian matrix at the current magnification for transformation from 3-D motion space $\{\boldsymbol{M}\}$ to u–v image plane in $\{\boldsymbol{C}\}$. The coordinates $u_P(t)$ and $v_P(t)$ represent the coordinates along the u-axis and v-axis, respectively, of the point projected onto the image plane at the time instant t for a tracked feature point. Similarly, u_{target} and v_{target} denote the coordinates along the u-axis and v-axis, respectively, corresponding to the projection of the initial values (initially positioned rotational target values) onto the image plane. T is the number of steps in one iteration.

In addition to the average position shift, we also define the maximum position shift $\mathrm{SFT}_{\mathrm{max}}$, and the standard deviation of position SD throughout the entire rotating process as follows:

$$\mathrm{SFT}_{\mathrm{max}} = \max_{1 \le t \le T} \{\mathrm{SFT}(t)\} \tag{17}$$

$$\mathrm{SD} = \sqrt{\frac{1}{T-1} \sum_{t=1}^{T} (\mathrm{SFT}(t) - \mathrm{SFT}_{\mathrm{avg}})}.. \tag{18}$$

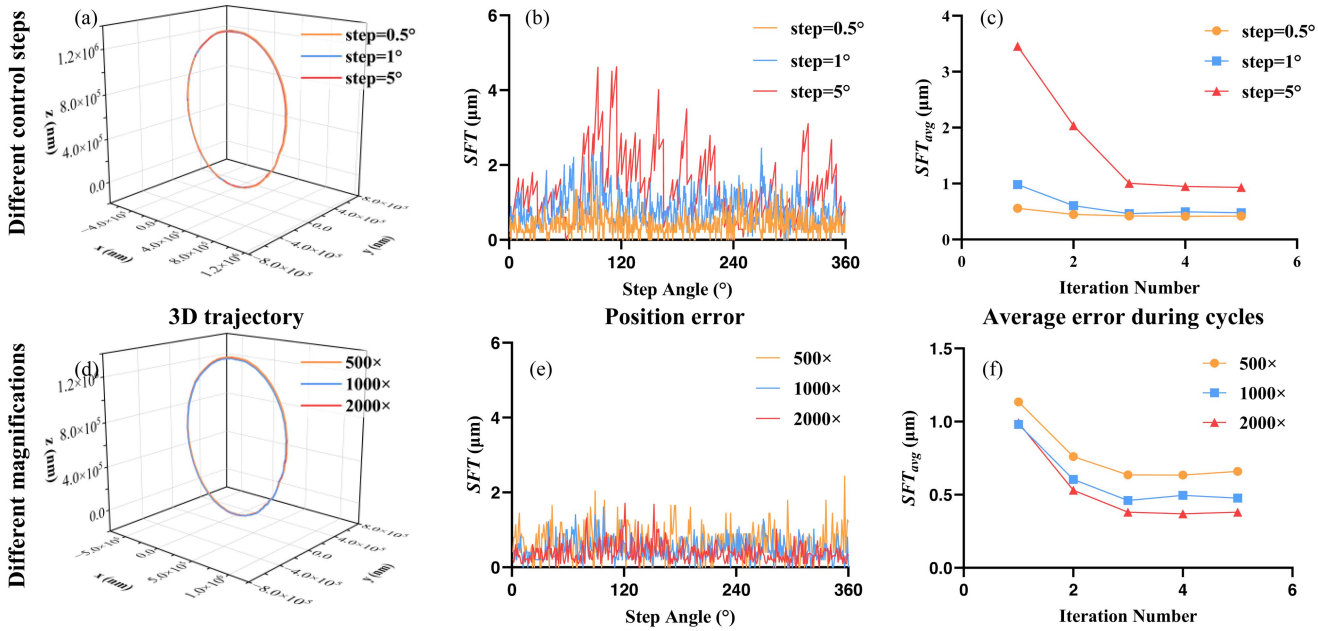

Fig. 6. Experimental results of the off-axis in-situ rotary manipulation at different magnifications and rotation control steps. For different step sizes of 0.5°, 1°, and 5°, and the same magnification of 1000×, (a)–(c) demonstrates the 3-D trajectory of linear nanopositioners, position error of tracked feature point on image plane, and convergence of average position error as the function of revolution. Under different magnifications 500×, 1000×, and 2000× with the fixed step size of 1° (d)–(f) demonstrates the 3-D trajectory of linear nanopositioners, position error of tracked feature point on image plane, and convergence of average position error as the function of revolution.

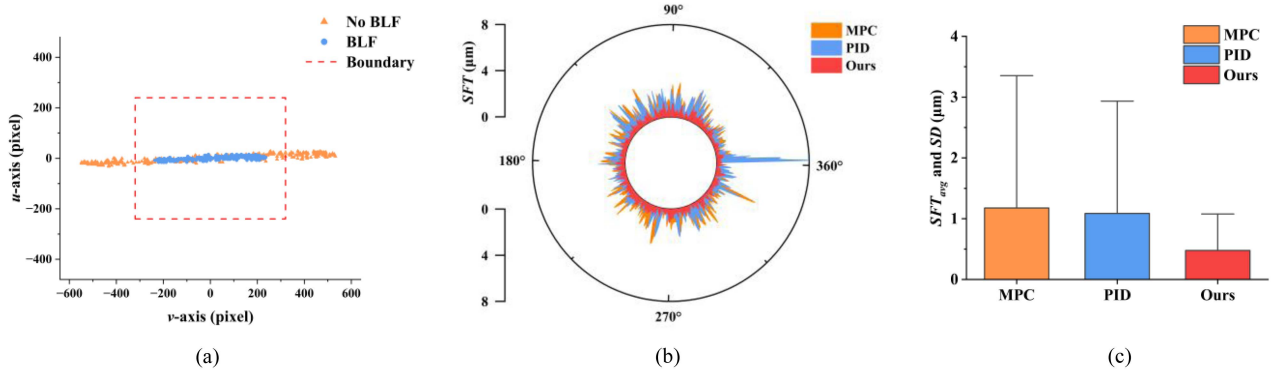

Fig. 7. Validation of BLF term, and comparative experiment results over control strategy with PID controller and MPC. (a) Scatter plot of the position of the tracked feature point positions steered by the controller with and without BLF term for the off-axis in-situ rotation with magnification of 500× and step size of 1°. The tracked feature point exceeds the boundary (FoV) without BLF term, while with BLF, the tracked feature point remained within FoV. (b) Comparison on position of tracked feature point of interest projected on image plane. (c) Comparative results of mean value and standard deviation over position error.

B. Experimental Results

1) Off-Axis In-Situ Rotation Under Different Step Sizes $\Delta\theta$ and Magnifications: The results of some representative experiments are depicted in Figs. 5 and 6 , which demonstrate a clear trend of convergence of the proposed controller across all three step sizes and magnification.

It is evident that larger step sizes result in greater positional errors with each rotation, due to the additional random noise of higher variance associated with larger control steps. On the other hand, a magnification of 500× introduces larger positional errors and higher oscillations. This is mainly because larger magnifications provide higher detection precision, which affects the feedback quality.

Further quantitative performance metrics of in-situ rotation is shown in Table I, encompassing the average position shift, maximum shift, and standard deviation. Overall, the proposed method not only enables rapid convergence and stability in various working conditions, but also exhibits more precise performance, particularly at smaller step sizes. Via extensive experiments, we see that the method achieves optimal result at a magnification factor of 2000× and a step size of 0.5°. In this scenario, the average position shift $\mathrm{SFT}_{\mathrm{avg}}$ decreases significantly, from 478.310 to 0.309 μm, representing a remarkable 99.935% improvement.

2) The Effectiveness of the BLF Term: In this experiment, the constraint k_b is selected as 75 000, which determined by the FoV [48 μm × 64 μm, see the red dashed line in Fig. 7(a)] at magnification of 2000×. However, for better illustration, the

TABLE I
EXPERIMENTAL RESULTS ON OFF-AXIS ROTATING CONTROL METHODS

Exp. No.	Control method	Magnification	Step angle	Round No.	Average position shift	Maximum position shift	Standard deviation
			$\Delta\theta$ (°)	/	SFT_{avg} (nm)	SFT_{max} (nm)	SD (nm)
1	None	/	1	/	478310	959032	290710
2	PID	1000	0.5	/	815	7603	750
3			1		1088	11736	1009
4			5		/	/	/
5	MPC	1000	0.5	/	822	3105	513
6			1		1176	4600	810
7			5		3725	10641	2600
8	Ours	500	0.5	1	724	2912	479
				5	553	1789	376
9			1	1	1135	4020	753
				5	660	2433	409
10			5	1	3763	10198	2476
				5	1131	2912	745
11		1000	0.5	1	558	1897	376
				5	417	1442	277
12			1	1	981	3800	648
				5	477	1613	289
13			5	1	3456	9833	2348
				5	931	3423	650
14		2000	0.5	1	538	2335	372
				5	**309**	**1342**	**233**
15			1	1	992	3354	697
				5	381	1456	254
16			5	1	3670	10050	2552
				5	1028	2648	904

magnification in the experiment is set to be 500×. The input in the first iteration is $\boldsymbol{u}(t, 1) = \boldsymbol{K}_0 \boldsymbol{w}(t, k)$ with $\boldsymbol{K}_0 = \text{diag}\{-0.1, -0.1, -0.1\}$. It shows that, without BLF term, the tracked feature point exceeded boundary, which indicates the cantilever went beyond FoV at the magnification of 2000×.

3) Comparison With Other Control Methods: To further underscore the superiority of ILC method, we conducted comparative analyses with PID and MPC. For the fairness of the comparison, the parameters of three methods were first tuned to achieve similar accuracy in the first round, at a magnification of 1000× and a control step of 1° (see Table I). Parameters for ILC are specified in Section IV-A with magnification of 1000× and step size of 1°. For PID controller, the proportional gain K_P, integral gain K_I, and derivative gain K_D are set as 0.8, 0.5, and 0.4. For model predictive controller, the state and terminal state weighting matrices are configured as diag{10, 10, 10}, while the input weighting matrix is determined as diag{1, 1, 1}.

The comparative results of the three controllers are illustrated in Fig. 7 and Table I, reflecting the superior precision of the proposed method at other magnifications and step sizes. As detailed in Table I, PID fail at the control step of 5° since it ran out of FoV in the first several steps. MPC achieves comparable tracking accuracy to the ILC method in control step of 0.5° and 1°, while at 5° increments, MPC exhibits significantly degraded performance, demonstrating around four times greater SFT_{avg} than ILC. This degradation of the performance arises because PID is model-free, while the performance of MPC heavily relies on the accuracy of the model. The ILC in this article effectively balances these aspects, demonstrating a commendable utilization of iterative nature of in-situ rotation and successfully learned the properties related to the machining error.

TABLE II
EXPERIMENTAL RESULTS ON RECONSTRUCTION

Control method	PSNR↑	SSIM↑	MSE↓
Ours	**27.6387**	**0.9206**	**0.0017**
PID	18.9718	0.7539	0.0127
MPC	16.2124	0.7520	0.0239

The bold values presented the highest performance in various metrices.

C. Application

High-magnification observation of microscale specimens through SEM has emerged as a critical research frontier, driving substantial advancements across multiple scientific disciplines. While conventional microscopy systems remain constrained to static single-view imaging, dynamic multiangle in situ characterization typically necessitates hardware modifications. By acquiring sequential SEM images during the rotation, we implement NeRF-based [40], [41] 3-D morphology reconstruction of atomic force microscope cantilevers. The reconstruction fidelity can provide enhanced spatial understanding for material analysis and robotic nanomanipulation applications.

As shown in Fig. 8, the 3-D morphology of the nanotube is reconstructed through implicit representation using the proposed control method, PID controller, and MPC technique, respectively. The proposed method achieves clear reconstruction with an average peak signal-to-noise ratio of 27.6387 dB, whereas PID- and MPC-based reconstructions display visual artifacts and edge distortions, especially near sample boundaries. Combined with the experimental results in Table II, the high precision of the in-situ rotation enabled by the proposed method is evident.

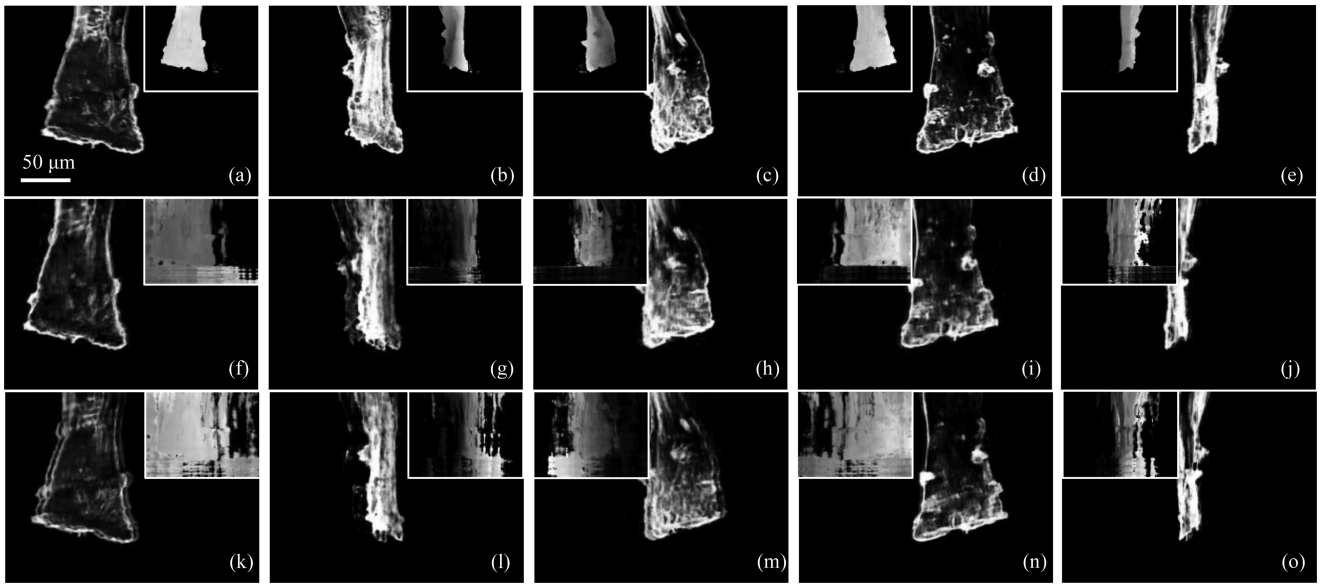

Fig. 8. (a)–(e) show the reconstruction results at novel views of 9°, 74°, 139°, 204°, and 268°, training from the SEM images captured using our in-situ rotating control method. (f)–(j) and (k)–(o) present the reconstruction results of images using PID and MPC controllers, respectively. Each image includes a corresponding depth map as a subgraph, where darker shades indicate closer proximity to the camera. The length of scale bar in each image is 50 μm.

Our algorithm, adapted from the NeRF codebase with minor modifications for SEM imaging protocols, utilizes 360 uniformly captured 1000× magnification nanotube images (90 for training and 270 for testing). The framework underwent 200 000 training iterations per reconstruction experiment, with validation error monitoring every 20 000 iterations. Implemented on a single NVIDIA 4070Ti Super GPU, the complete training process required approximately 6 h.

D. Discussion

This article presents a superior approach to high-precision off-axis in-situ rotation using a classic nanorobot within SEM, highlighting key advantages in modeling and control.

First, the nanorobot, comprising three orthogonal linear nanopositioners and a rotary nanopositioner at the end joint, imposes no restrictions on rotation axis direction, enabling flexible system configurations and complex nanomanipulation.

Second, unlike conventional methods requiring additional hardware, our approach achieves rotational manipulation through a control-oriented discrete-time SSM based on kinematics rather than dynamics. This enables real-time position shift compensation via outer-loop control and extends to similar nanorobotic systems for repetitive tasks.

Third, the proposed control method ensures iterative convergence (ILC) and state boundedness (BLF), providing a computationally efficient and theoretically guaranteed solution for high-precision operations in confined spaces. Experimental results show that compensation reduces the average displacement of the cantilever from 478.310 to 0.309 μm.

Finally, in practical, the control algorithm is running on a laptop, with CPU i7 10700H and 16 GB RAM and referenced runtimes of our method and PID are less than 1 ms, while MPC costs about 3 ms. Regarding the control code for the article, it is integrated into an interactive application written in C++ using Qt. The code is contained in the GitHub as following link: https://github.com/FactspacX/ILC-BLF_Insitu_Control.git.

V. Conclusion

In this article, we have demonstrated a high-precision off-axis in-situ rotation method for a classic nanorobot within an SEM environment. The primary challenge lies in the restricted workspace, limited FOV, and DoF, coupled with significant position shifts due to end-effector misalignment. To address these issues, we propose a novel control-oriented model together with an IL–BLF-based controller that effectively leverages the repeatability of in-situ rotation, eventually achieving asymptotically converged precision, with an average deviation of 0.309 μm. The extensive experimental validation, including comparative analyses with PID control and MPC, underscores the stability, reliability, and superiority of our proposed strategy. This article represents a significant advancement in the field of high-precision nanorobotic manipulation, offering a robust and hardware-modification-free solution that can be readily adapted to a wide range of nanomanipulation tasks.

References

[1] P. Wang, H. Lu, and Y. Shen, "Flexible 3-D helix fabrication by in-situ SEM micromanipulation system," *IEEE Trans. Ind. Electron.*, vol. 67, no. 7, pp. 5565–5574, Jul. 2020.
[2] A.A.G. Requicha, "Nanorobots, NEMS and nanoassembly," *Proc. IEEE*, vol. 91, no. 11, pp. 1922–1933, Nov. 2003.
[3] H. Mei et al., "Nano manipulation and assembly of silver nanowires in situ for advanced fabrication," *ACS Appl. Nano Mater.*, vol. 7, no. 18, pp. 21590–21602, 2024.
[4] U. Dey et al., "Path planning of micromanipulators inside an SEM and 3D nanomanipulation of CNTs for nanodevice construction," *Mechatronics*, vol. 101, 2024, Art. no. 103196.

[5] S. Zhuang, C. Dai, G. Shan, C. Ru, Z. Zhang, and Y. Sun, "Robotic rotational positioning of end-effectors for micromanipulation," *IEEE Trans. Robot.*, vol. 38, no. 4, pp. 2251–2261, Aug. 2022.
[6] T. Cui et al., "Single-cell level investigation of microbiologically induced degradation of passive film of stainless steel via FIB-SEM/TEM and multimode AFM," *Corrosion Sci.*, vol. 206, 2022, Art. no. 110543.
[7] W. Shang, H. Lu, Y. Yang, and Y. Shen, "7-DoFs rotation-thrust microrobotic control for low-invasive cell pierce via impedance compensation," *IEEE/ASME Trans. Mechatron.*, vol. 27, no. 6, pp. 5095–5106, Dec. 2022.
[8] T. Fujiwara, M. Nakajima, A. Ichikawa, K. Ohara, Y. Hasegawa, and T. Fukuda, "Bending of multi-graphene by nanomanipulation assisted with electron beam irradiation for box structure," in *Proc. 41st Annu. Conf. IEEE Ind. Electron. Soc.*, 2015, pp. 02578–02583.
[9] M. Nakajima, M. Takeuchi, T. Fukuda, Y. Hasegawa, and Q. Huang, "In situ nanomanipulation with 3D SEM-CT observation inside environmental SEM," in *Proc. Int. Symp. Micro-NanoMechatron. Hum. Sci.*, 2015, pp. 1–2.
[10] W. Wan, H. Lu, and Y. Shen, "Rotational nanorobotic manipulation system with increment alignment method for multi-directional defect characterization inside SEM," in *Proc. IEEE/RSJ Int. Conf. Intell. Robots Syst.*, 2017, pp. 1901–1906.
[11] H. Lu et al., "Nanorobotic system iTRo for controllable 1D micro/nano material twisting test," *Sci. Rep.*, vol. 7, no. 1, pp. 1–11, 2017.
[12] H. Lu, F. Xue, W. Wan, and Y. Shen, "Investigation of scaling effect of copper microwire based on in-situ nanorobotic twisting inside SEM," in *Proc. IEEE Int. Conf. Robot. Automat.*, 2018, pp. 3461–3466.
[13] Y. Shen, M. Nakajima, Z. Zhang, and T. Fukuda, "Dynamic force characterization microscopy based on integrated nanorobotic AFM and SEM system for detachment process study," *IEEE/ASME Trans. Mechatron.*, vol. 20, no. 6, pp. 3009–3017, Dec. 2015.
[14] P. Gao, J. Gao, T. Zou, and W. Rong, "The measurement of the elastic modulus and kinetic friction coefficient of long nanowires by the microforce probe in the SEM combined with finite element simulation," in *Proc. IEEE 4th Int. Conf. Nanoscience Technol.*, 2021, pp. 58–63.
[15] Huiyang Ding and Li Ma, "Visual servoing-based nanorobotic system for automated electrical characterization of nanotubes inside SEM," *Sensors*, vol. 18, no. 4, 2018, Art. no. 1137.
[16] J. Qu et al., "An SEM-based nanomanipulation system for multiphysical characterization of single InGaN/GaN nanowires," *IEEE Trans. Automat. Sci. Eng.*, vol. 20, no. 1, pp. 233–243, Jan. 2023, doi: 10.1109/TASE.2022.3146486.
[17] Feiling Shen et al., "Structure characterization of interior invisible single grain boundary by nanorobot pick-and-place grain in bulk ZnO under SEM," *Mater. Lett.*, vol. 324, 2022, Art. no. 132777.
[18] Quan Yang et al., "Electrical conductivity of multiwall carbon nanotube bundles contacting with metal electrodes by nano manipulators inside SEM," *Nanomaterials*, vol. 11, no. 5, 2021, Art. no. 1290.
[19] C. Han, L. Zhang, and Z. Yang, "Division of CNT placement meta-task for micro-nano robotic manipulator," in *Proc. IEEE Int. Conf. Manipulation, Manuf. Meas. Nanoscale*, 2021, pp. 71–76.
[20] N. Marturi, B. Tamadazte, S. Dembélé, and N. Piat, "Visual servoing-based depth-estimation technique for manipulation inside SEM," *IEEE Trans. Instrum. Meas.*, vol. 65, no. 8, pp. 1847–1855, Aug. 2016.
[21] T. Kasaya, H. Miyazaki, S. Saito, and T. Sato, "Micro object handling under SEM by vision-based automatic control," in *Proc. IEEE Int. Conf. Robot. Automat.*, 1999, pp. 2189–2196.
[22] Y. Shen, W. Wan, H. Lu, T. Fukuda, and W. Shang, "Automatic sample alignment under microscopy for 360° imaging based on the nanorobotic manipulation system," *IEEE Trans. Robot.*, vol. 33, no. 1, pp. 220–226, Feb. 2017.
[23] W. Shang, M. Zhu, H. Ren, and X. Wu, "Centering of a miniature rotation robot for multi-directional imaging under microscopy," *IEEE Trans. Nanotechnol.*, vol. 19, pp. 17–20, 2020.
[24] H. Lu, W. Shang, H. Xie, and Y. Shen, "Ultrahigh-precision rotational positioning under a microscope: Nanorobotic system, modeling, control, and applications," *IEEE Trans. Robot.*, vol. 34, no. 2, pp. 497–507, Apr. 2018.
[25] X. Xue et al., "Time-dependent microstructural evolution mechanisms of twisted carbon nanotube fibers under tension and relaxation," *Int. J. Plast.*, vol. 22, 2021, Art. no. 102866.
[26] T. Zhang, H. Ren, G. Li, P. Wang, W. Shang, and Y. Shen, "High-precise metallic helical microstructure fabrication by rotational nanorobotic manipulation system with tilted mandrel compensation," *IEEE/ASME Trans. Mechatron.*, vol. 29, no. 1, pp. 214–223, Feb. 2024.
[27] W. Young Song, K. Young Jung, and B. C. Park, "Accuracy improvement of protrusion angle of carbon nanotube tips by precision multiaxis nanomanipulator," *Rev. Sci. Instrum.*, vol. 76, no. 2, 2005, Art. no. 025107.
[28] Z. Yang et al., "Mechatronic development and vision feedback control of a nanorobotics manipulation system inside SEM for nanodevice assembly," *Sensors*, vol. 16, no. 9, 2016, Art. no. 1479.
[29] Y. Yang, T. Li, X. Fu, Z. Sun, Y. F. Li, and S. Liu, "Zooming-free hand-eye self-calibration for nanorobotic manipulation inside SEM," *IEEE Trans. Nanotechnol.*, vol. 22, pp. 291–300, 2023.
[30] S. Briot, F. Chaumette, and P. Martinet, "Revisiting the determination of the singularity cases in the visual servoing of image points through the concept of hidden robot," *IEEE Trans. Robot.*, vol. 33, no. 3, pp. 536–546, Jun. 2017.
[31] W. Shang, H. Lu, Y. Yang, and Y. Shen, "7-DoFs rotation-thrust microrobotic control for low-invasive cell pierce via impedance compensation," *IEEE/ASME Trans. Mechatron.*, vol. 27, no. 6, pp. 5095–5106, Dec. 2022.
[32] H. Zhang, X. Fu, S. Liu, and Y. Wang, "Iterative learning embedded composite model reference adaptive control for off-axis in-situ rotation in nanorobotic manipulation," *IEEE Control Syst. Lett.*, vol. 8, pp. 291–296, 2024.
[33] S. Liang et al., "Model predictive control with obstacle avoidance for inertia actuated AFM probes inside a scanning electron microscope," *IEEE Robot. Automat. Lett.*, vol. 6, no. 2, pp. 382–388, Apr. 2021.
[34] S. Dumitru and A. Craifaleanu, "Kinematic model of an anthropomorphic robotic arm," *Ann. Fac. Eng. Hunedoara*, vol. 22, no. 1, pp. 55–60, 2022.
[35] Z. Haichao and L. Weiyao, "Robust output regulation problem with prescribed performance for nonlinear strict feedback systems," *J. Syst. Eng. Electron.*, vol. 34, no. 4, pp. 1033–1041, Aug. 2023.
[36] G. Zhai, E. Tian, Y. Luo, and D. Liang, "Data-driven optimal output regulation for unknown linear discrete-time systems based on parameterization approach," *Appl. Math. Comput.*, vol. 461, 2024, Art. no. 128300.
[37] M. B. Rhudy and Y. Gu, "Online stochastic convergence analysis of the Kalman filter," *Int. J. Stochastic Anal.*, vol. 2013, no. 1, 2013, Art. no. 240295.
[38] Z. Zhuang, H. Tao, Y. Chen, V. Stojanovic, and W. Paszke, "An optimal iterative learning control approach for linear systems with nonuniform trial lengths under input constraints," *IEEE Trans. Syst., Man, Cybern.: Syst.*, vol. 53, no. 6, pp. 3461–3473, Jun. 2023.
[39] C. Xu, J. Su, T. Wang, Y. Zhang, and A. Yu, "Improved Canny edge detection operator," in *Proc. 7th Int. Conf. Commun. Inf. Syst.*, 2023, pp. 135–140.
[40] B. Mildenhall et al, "NeRF: Representing scenes as neural radiance fields for view synthesis," *Commun. ACM*, vol. 65, no. 1, pp. 99–106, 2021.
[41] X. Fu et al., "NanoNeRF: Robot-assisted nanoscale 360° reconstruction with neural radiance field under scanning electron microscope," in *Proc. IEEE/RSJ Int. Conf. Intell. Robots Syst.*, 2024, pp. 1343–1348.

Xiang Fu received the B.S. degree in computer science from ShanghaiTech University, Shanghai, China, 2022. He is currently working toward the Ph.D. degree in intelligent robotics with the Advanced Micro-Nano Robots Lab, ShanghaiTech University, Shanghai, China.

His research interests include visual-servoing control, nanorobotic manipulation, 3-D reconstruction, and embodied intelligence.

Heng Zhang is currently working toward the doctoral degree in intelligent robotics with the Multi-Agent and Intelligent Control Lab, ShanghaiTech University, Shanghai, China.

His research interests include adaptive control, iterative learning control, and data-driven modeling.

Yuting Yang is currently working toward the master's degree in intelligent robotics with the Advanced Micro-Nano Robot Lab, ShanghaiTech University, Shanghai, China.

Her research interests include visual servo control, image processing, and nanorobotic manipulation.

Song Liu received the B.S. degree in sensing technology and instrumentation from the Shandong University, Jinan, China, in 2012, and the Ph.D. degrees in control science and engineering from the University of Chinese Academy of Sciences, Beijing, China, and the City University of Hong Kong, Hong Kong, in 2017.

He is curremtly serving as a Tenure-Track Assistant Professor with the ShanghaiTech University, Shanghai, China. His research interests include ultrasonic MEMS, acoustic holography, nanorobotic manipulation, and robot learning.

Yang Wang (Member, IEEE) received the B.Eng. degree in electrical and electronic engineering from the Tongji University, Shanghai, China, in 2013, and the M.Sc. and Ph.D. degrees in control systems from the Imperial College London, London, U.K., in 2014 and 2019, respectively.

From 2014 to 2019, she held visiting scholar positions with the University of Cambridge, Cambridge, U.K., and the Ohio State University, Columbus, OH, USA. Since 2020, she has been a tenure-track Assistant Professor with the School of Information Science and Technology, ShanghaiTech University, Shanghai, China. Her research interests include intersection of nonlinear system and adaptive control theory, with applications in covering robotic fish, quadrotors, etc.